Growth of Fe-BDC Metal Organic Frameworks onto functionalized Si (111) surfaces

Hongye Yuan, Weichu Fu, Nadia Soulmi, Christian Serre, Nathalie Steunou, Michel Rosso, Catherine Henry de Villeneuve

RESEARCH ARTICLE

Growth of Fe-BDC Metal Organic Frameworks onto functionalized Si (111) surfaces

Hongye Yuan [§ a], Weichu Fu [§ a], Nadia Soulmi [a], Christian Serre [b], Nathalie Steunou [c], Michel Rosso [a], Catherine Henry de Villeneuve [a]*

[a] H. Yuan, W. Fu, N. Soulmi, M. Rosso, C. Henry de Villeneuve*,
Laboratoire de Physique de la Matière Condensée
CNRS, Ecole Polytechnique, Institut Polytechnique de Paris
91120 Palaiseau, France.
Corresponding author: catherine.henry-de-villeneuve@polytechnique.edu

H. Yuan (current address)
State Key Laboratory for Mechanical Behavior of Materials
Shaanxi International Research Center for Soft Matter, School of Materials Science and Engineering,
Xi'an Jiaotong University, Xi'an 710049, P. R. C.

N. Soulmi (current address)
Technocentre Renault, 78084 Guyancourt, France.

[b] C. Serre,
Institut des Matériaux Poreux de Paris, Ecole Normale Supérieure, ESPCI Paris, CNRS PSL University, 75005, Paris, France.

[c] N. Steunou,
Institut Lavoisier de Versailles, UMR CNRS 8180, Université de Versailles St Quentin en Yvelines, Université Paris Saclay, 78000 Versailles, France.

[§] These authors contributed equally to the work.

Supporting information for this article is given via a link at the end of the document.

Abstract: The realization of metal organic frameworks (MOFs) layers onto solid surfaces is a prerequisite for their integration into devices. This work reports the direct growth of Fe^{3+}/benzene di-carboxylate MOFs onto functionalized silicon surfaces, compatible with a wide range of MOF synthesis conditions. The co-nucleation and growth of different crystalline phases are evidenced, whose coverage depends on the surface chemistry and/or the solution composition. Three structural phases – the cubic MIL-101(Fe), a hexagonal phase with a structure close to MOF-235 and a MIL-53(Fe) with a monoclinic symmetry - are identified through characteristic crystal shapes and their structural parameters inferred from X-Ray Diffraction. In addition to the oriented growth of 3D crystallites, the formation of two-dimensional MIL-101 nano-crystallites or thin layers/islands exhibiting extended monocrystalline domains with (111) texture is also demonstrated through high-resolution Atomic Force Microscopy. Post-synthesis treatments reveal a weak adhesion of the hexagonal phase indicating a different surface anchoring.

Introduction

Metal organic frameworks (MOFs) are a family of porous and crystalline hybrid materials obtained by self-assembly of metal cations and organic linkers.[1] These solids exhibit a high porosity often superior to that of well-known inorganic porous materials (zeolites, carbons or porous silica) as well as versatile structural (pore size and shape) and physico-chemical properties tunable by the choice of the precursors (metal and/or linker). During the past two decades most studies have been focused on the design of new MOFs, their large scale production, and new synthesis strategies[2] to meet the demands of diverse potential applications (separation[3], catalysis[3h, 4], sensors[3h, 5], biomedicine[5f, 5g, 6]...). More recently, particular efforts have been devoted to their integration into devices for sensing or electronic applications.[5h, 5i, 7] If numerous proofs of concepts have been reported, the design of MOF-based devices still faces numerous technical issues. Among others, the realization of MOF thin layers combining controlled morphology and structural properties while providing the desired functionality still remains an important challenge.

Within this context the direct growth in liquid phase onto functionalized surfaces appears as a very attractive approach to prepare MOF layers with targeted properties. A wide choice of soluble precursors is available thus permitting the preparation of a large variety of MOFs. On the other hand, surface functionalization is anticipated to be a key issue to promote heterogeneous nucleation and surface growth and to improve surface adhesion. Examples of the growth of Cu-based MOF layers of high crystalline quality, with specific texture and tunable thickness are reported on gold substrates functionalized by a self-assembled monolayer (SAM).[8],[9] Because of the limited stability of the SAMs, this approach is however restricted to the growth of MOFs whose synthesis can be performed in "soft" conditions i.e. at temperature close to room temperature (RT) and only in suited solvents.

The MOFs investigated in this work are Fe-carboxylate based MOFs obtained from Fe^{3+} cations and 1,4-benzene dicarboxylic acid (BDC) whose synthesis in homogeneous phase (water or dimethyl formamide (DMF)) requires usually high temperature (~100°C or above) and is performed in solvothermal or reflux conditions. The Fe-BDC system is characterized by a remarkable polymorphism with benchmark MOFs such as MIL-101[10], MIL-88B[11] or MOF-235[12], MIL-53[13] and MIL-68[14] as well as recently reported new polymorphs[15] (MIL stands for Material of Institut Lavoisier). These different structural phases - obtained in homogeneous phase by adjusting the synthesis conditions -

exhibit different crystalline structures and porosities (pore size and shape) with either trimeric building units (MIL-88B, MIL-101, MOF-235) or corner-sharing chains of metal octahedra (MIL-53 and MIL-68). Some of these MOFs exhibit a rigid framework (MIL-101, MOF-235, MIL-68) while MIL-88B and MIL-53 correspond to flexible networks for which reversible variations of structural parameters are observed upon release or uptake of guest molecules, associated in the case of MIL-53 with changes of symmetry.[13b, 16] MIL-88B and MOF-235 are two hexagonal phases differing mainly through the type of counter-anion.[12, 16a, 16c] The different Fe-BDC polymorphs have different porosities: mesoporous cages (29 -34 Å) for MIL-101 and 1D microporous channels (6 -20 Å) for the others. A compilation of the 3D structures of the different Fe-BDC polymorphs can be found in ref.[15]

The versatility of the structural and physico-chemical properties of Fe-carboxylate MOFs coupled to their optical properties (photo-activity) make these materials interesting for numerous applications (gas separation[17], pollutant uptake and photo-degradation[18], chem/bio sensing[18e, 19], water splitting[20], energy storage[21]). Their shaping on solid surfaces is generally achieved by deposition/precipitation of crystallites grown in homogeneous phase or using Fe oxide solid precursor as template[2b]. The as-prepared layers are polycrystalline, their structural properties (coverage and density, thickness, crystalline quality or orientation) are difficult to control and their adhesion is very often an issue.

Very few examples of *direct* surface growth of Fe-carboxylate MOFs are reported in the literature. Scherb et al. investigated the growth of Fe-BDC MOF onto gold surfaces functionalized with carboxylic acid SAM.[16c, 22] To avoid SAM damaging, the growth is performed at room temperature by immersing the functionalized gold surfaces for several days in a filtered and pre-heated liquor solution, obtained after solvothermal synthesis of MIL-53 bulk material (DMF, 150°). Using this procedure, they report the surface growth of a structural phase - oriented MIL-88B crystallites with (001) texture – different from that obtained in the homogeneous phase. Using *in situ* XRay Diffraction (XRD) they demonstrated the structural flexibility of the surface grown MIL-88B crystallites upon guest sorption or desorption.

In this work Fe-BDC MOFs are grown directly by exposing functionalized silicon surfaces into freshly prepared DMF solution containing Fe^{3+} and BDC precursors. The Si surfaces are beforehand functionalized by covalent grafting of a ω-functionalized organic monolayer (ML) onto hydrogenated Si surfaces using hydrosilylation reaction.[23] Compared to SAM on gold systems, the as-functionalized Si surfaces exhibit a greater chemical and thermal stability (up to 200°C) resulting from a robust ML anchoring through covalent Si-C bonds.[24] This robust covalent anchoring makes these functionalized surfaces compatible with a large range of MOF synthesis conditions. Various synthesis conditions were investigated including a wide temperature range (up to 150°C), various precursor concentrations and growth times (few hours to 24 hours). The co-nucleation and growth of different crystalline phases is evidenced. Their nature and their structural parameters are discussed on the basis of Scanning Electron Microscopy (SEM) and high-resolution atomic Force Microscopy (AFM) imaging, XRay Diffraction (XRD) characterizations and structural model.

Results and Discussion

Results

As-prepared samples

An overview of Fe-BDC MOFs obtained on surfaces modified with a carboxylic acid terminated ML (Si-COOH surfaces) is displayed in **Fig.1**. The three samples A, B, C were prepared in similar conditions (growth for 24h at 90°C) using different precursor concentrations or ratios $R = C_{BDC} / C_{Fe}$. In all cases the SEM images show the growth of faceted particles and/or layers indicating the formation of crystalline phases. Crystallites with different shape/habitus are observed suggesting – at first glance – the growth of different structural phases or different textures. The different types of crystalline structures are labeled on the images (right column): **O** for the octahedra, **FP** for the flat prism-like crystallites with hexagonal irregular shape lying flat or standing vertically or almost vertically on the surface, **HPy** for the oriented hexagonal pyramids, **TPy** for the tetrahedral pyramids and **TP** for the triangular particles.

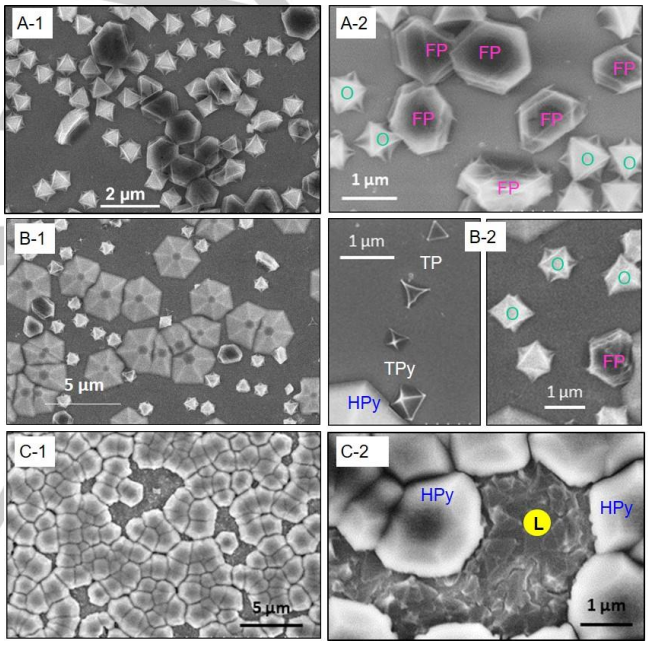

Figure 1. SEM images showing the different types of Fe/BDC crystalline phases obtained on Si-COOH surfaces: Octhaedra (**O**), horizontal or vertical Flat Prisms (**FP**), oriented Hexagonal Pyramids (**HPy**), tetrahedral pyramids (**TPy**) and triangular particles (**TP**) on samples A and B (top and middle), and close packed Hexagonal Pyramids (**HPy**) and a continuous faceted layer (**L**) on sample C (bottom). Synthesis conditions: temperature T= 90°C, growth time = 24h, $C_{Fe} = 2C_{BDC} = 50$ mM (sample A); $C_{Fe} = C_{BDC} = 25$ mM (sample B); $C_{Fe} = C_{BDC} = 50$ mM (sample C).

Variable amounts of each type of crystallite are observed depending on the surface chemistry and/or the precursor ratio in solution R. On Si-COOH surfaces, in case of metal excess (R = 0.5, **Fig.1 A1, A2**), octahedra **O** and prisms **FP** are the dominant crystalline phases. In some cases one can observe that neighbor crystallites merge together leading to the formation of 2D flat islands. Remarkably, in condition of metal excess a very low density of hexagonal pyramids **HPy** is observed with respect to the density of **O** and **FP** crystallites (about 5 10^4 **HPy**

crystallites.cm^{-2} against about 3.2 10^7 **O** crystallites.cm^{-2} and about 1.3 10^7 **FP** crystallites.cm^{-2} on sample A). Much higher densities of **HPy** crystallites are obtained when increasing the linker concentration (R ≥ 1). In this case, the SEM images show more or less densely packed **HPy** co-existing with other structural phases: **O**, **FP** as well as triangular **TP** or tetrahedral **TPy** crystallites on sample B (**Fig.1 B1, B2**), and a continuous faceted layer **L** on sample C (**Fig.1 C1, C2**).

Interestingly our studies show that the oriented growth of hexagonal crystallites *i)* is favored in presence of BDC excess in solution (R = C_{Fe}/C_{BDC} ≥ 1) and ii) is solely observed on surfaces functionalized with terminal carboxylic acid groups. In order to investigate the effect of surface chemistry, the growth was also studied on surfaces with other coordinating surface groups i.e. on oxidized surface with hydroxyl terminal groups (Si-Ox) or on Si surfaces with pyridyl groups (Si-Pyr)[25]**.** These studies show the growth of octahedra (**O**) and irregular prisms (**FP**) whatever the precursor concentration, but never the growth of **HPy** crystallites. Further, it should be emphasized that *no growth* is observed in absence of coordinating surface group (Si surfaces modified by alkyl monolayer with methyl terminal groups[23c, 26]).[27]

The crystallite thickness was determined from the AFM images (**Fig.SI-2**) and the volume of matter corresponding to each type determined from their size and respective density (**Fig.2)**.

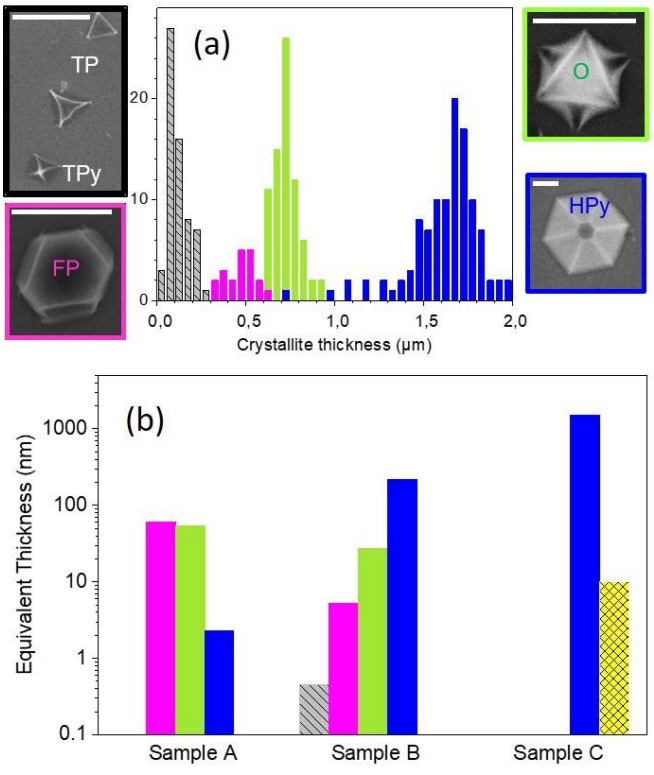

Figure 2. (top) Height distribution of the **O**, **FP**, **HPy**, **TPy** and **TP** crystallites measured on AFM images (sample B). **(bottom)** Amount of matter corresponding to the different crystallites on the samples A, B and C. The color code is the same for both plots: blue correspond to **HPy**, green to **O**, pink to **FP**, hatched grey to **TP** and **TPy**, hatched yellow to the faceted layer **L**. The equivalent thicknesses were determined from the mean crystallite density and their mean size (as determined from SEM and AFM). Note the log scale on the Y axis. The scale bar (in white) on the SEM images represents 1 µm.

In all cases the **HPy** crystallites represent the dominant phase in terms of amount of matter on the surface even in conditions their nucleation is not favored (i.e. in the case of metal excess in solution), indicating a much faster growth kinetics for this phase.

Besides the crystallites observed on the SEM images, much smaller nano-particles exhibiting well specific structural features were evidenced by AFM (**Fig.3a-b**). The particles are flat 2D structures with a thickness of about 4.2 nm and a lateral size around 100 nm. On their topmost surface, high resolution images reveal the presence of a hexagonal pore network with a mean pore distance of about 6 nm (**Fig. 3c-d**).

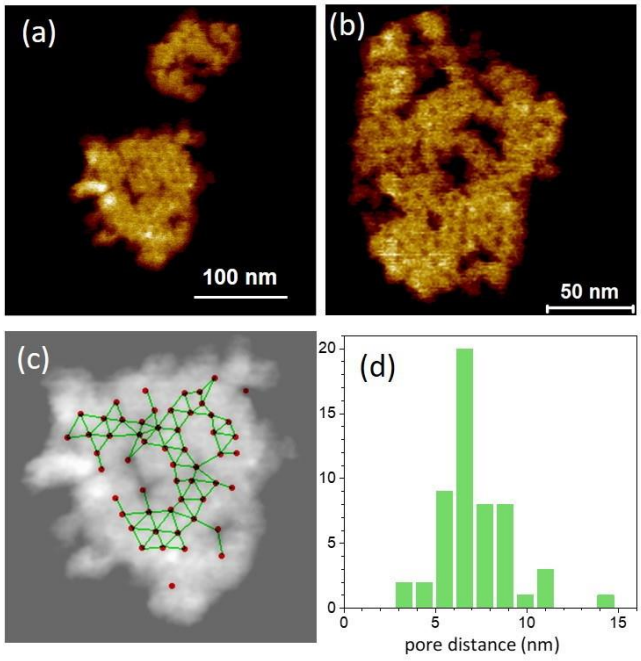

Figure 3. **(a, b)** High resolution AFM images of 2D nanoparticles with ordered pore network (dark spots) on their topmost surface. The particle thickness is ~ 4.2 nm. **(c, d)** Results of image processing pointing out the hexagonal symmetry of the pore network with a characteristic mean pore distance of ~ 6 nm.

XRD patterns (Bragg Brentano) of samples A, B, and C are displayed in **Fig.4a** and **Fig.5**. The XRD patterns are dominated by the presence of a couple of intense and narrow peaks at 2θ = 9.64° and 2θ = 19.35° (**Fig.4a**), but also show the presence of others peaks of much lower intensity (**Fig.5**). The peak positions are indicated in Table 1. The characterizations of a large panel of samples prepared in different conditions show that the presence of the two peaks at 2θ = 9.64° and 2θ = 19.35° is correlated to the presence of **HPy** crystallites on the surfaces. Quantitatively, their intensity scales linearly with the amount of matter corresponding to these crystallites (**Fig.4b**) allowing for assigning them to this hexagonal phase.

The peaks at low angles (2θ < 4°) can be unambiguously attributed to the MIL-101 phase which is the sole structural Fe-BDC phase giving rise to Bragg reflections within this angular range. For samples A and C, the peaks are very weak and are superimposed on a broad band which suggests the formation of small size particles or a poorly crystalline phase.

Except the peaks assignable to MIL-101 (green index) or to the **HPy** crystallites (blue index), several other peaks are also observed (labelled with stars or triangles). Their assignment is not

straightforward due to the known flexible character of several Fe-BDC polymorphs leading to variable possible peak positions. Their assignment will be further discussed in the discussion.

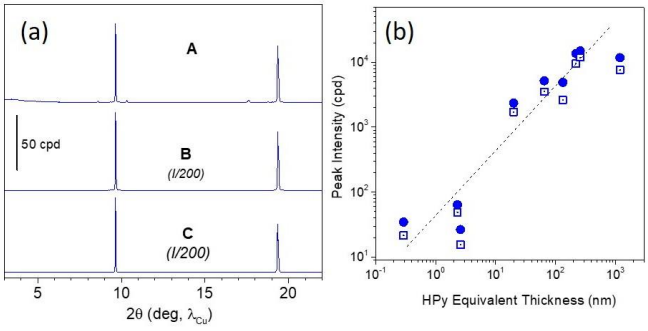

Figure 4: **(a)** XRD patterns (Bragg Brentano) of as-prepared samples A, B and C. **(b)** Peak intensity as a function of the equivalent thickness of the **HPy** crystallites. The equivalent thicknesses were calculated from the **HPy** crystallites density and size measured on SEM and AFM images. The filled dots and open squares correspond to the intensity of the peaks at 2θ = 9,64° and 2θ = 19,35° respectively. Note the linear scaling over three orders of magnitude. The dashed line is plotted to guide the eye.

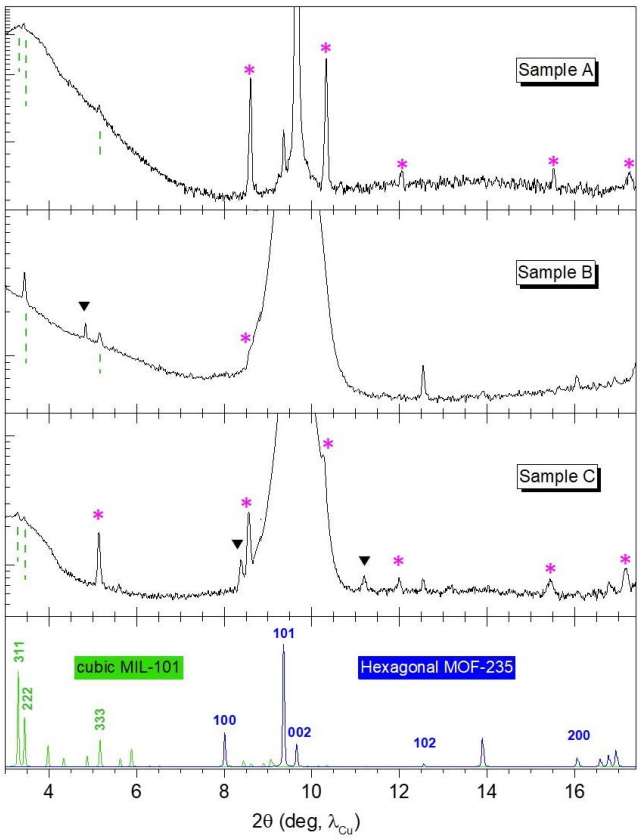

Figure 5. Zoom (Y axis, logarithmic plot) on XRD patterns of Fig.4a. The experimental patterns (black plots) are compared to the PXRD patterns of MIL101 (green plot) and of a MOF-235 type hexagonal phase (blue plot, see discussion). Peaks matching none of the Bragg peaks corresponding to these two structural phases (position and/or relative intensity) are labeled with pink stars or black triangles. See discussion for the peak assignment.

Table 1. Peak position and assignment. See discussion for the peak assignment.

2θ (λCu)			Bragg Reflections		
Sample A	**Sample B**	**Sample C**	MIL-101 cubic	Hexagonal phase	MIL-53 monoclinic
3.29°		3.28°	(311)		
3.44°	3.44°	3.43°	(222)		
	▾4.8°				
5.16°	5.16°	*5.14°	(333)		*(100)
		▾8.39°			
*8.59°	*8.6°	*8.55°			*(110)
9.35°				(101)	
9.65°	9.65°	9.65°		(002)	
*10.32°	*10.3°	*10.27°			*(200)
		▾11.2°			
*12.04°	*12°	*11.98°			*(001)
	12.5°	12.54°		(102)	
*15.5°	*15.4°	*15.43°			*(300)
		16.04°		(200)	
*17.24°	*17.1°	*17.15°			*(220)
19.37°	19.37°	19.37°		(004)	

Effect of additional rinsing

Fig.6 displays SEM images of B-type or A-type samples, after additional rinsing in DMF or ethanol (EtOH). The two samples in **Fig.6a** and **Fig.6b** were prepared using synthesis conditions in which the surface nucleation of oriented hexagonal **HPy** crystallites is favored (R = 1, sample B-type) and then rinsed according to the same procedure i. e. by immersion in DMF (**Fig.6a**) or EtOH (**Fig.6b**) at 90°C for 2h.

After additional rinsing in DMF (synthesis solvent) at a temperature close to that used for the synthesis, the SEM images reveal only minor changes (**Fig.6a**). Cracks are observed on a few number of **HPy** crystallites but globally their density and size remain similar to that before the rinsing. Conversely drastic changes are observed on a similar sample after rinsing in EtOH. In this case the SEM images reveal the disappearance of almost all the **HPy** crystallites (**Fig.6b**). After rinsing only few residues/broken pieces that can be identified as possible fragments of the previously existing **HPy** are still present on the surface.

The same behavior is observed for C-type samples (high density of **HPy**). In this case also, a short time rinsing in EtOH (soxhlet rinsing) leads to the removal of almost all the **HPy** crystallites. After rinsing, the SEM images only show the presence of 2D islands corresponding to the dense crystalline layer (**L**) present in between the **HPy** crystallites on the as-prepared samples (**Fig.SI-4.3**).

Comparatively a much greater stability/stronger anchoring is observed for the other structural phases (octahedra **O, FP** crystallites) (**Fig.6c)**. Even after prolonged rinsing (24h) in hot EtOH, no significant evolution of their density or their size is observed. Similar behaviors were observed for these crystallites whatever the synthesis conditions.

The weak anchoring of **HPy** crystallites is confirmed by XRD. After rinsing in EtOH the XRD patterns systematically reveal a huge decrease of the intensity of the couple of peaks at 2θ = 9.64° and 2θ = 19.35° assigned to these crystallites, sometimes their total disappearance. When still present, a shift of their position to lower angle is observed, indicating a modification of the structural parameters of the **HPy** fragments/residues remaining on the surface (**Fig.SI-4**).

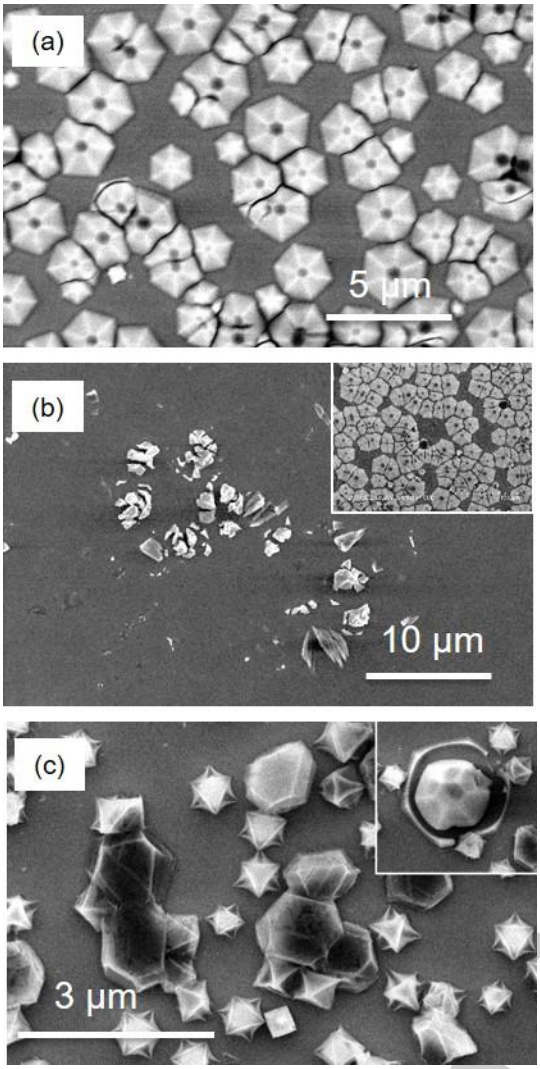

Figure 6. SEM images of Fe/BDC samples after additionnal rinsing. **(a, b)** B-type samples (majority of **HPy)** after 2h rinsing in DMF **(a)** or in ETOH **(b)** at 90°C. (c) A-type sample (with a majority of **O** and **FP** crystallites) after 24h EtOH soxhlet rinsing. The insert in **(b)** shows the surface morphology before the rinsing, for comparison. The insert in **(c)** shows the morphology change of one **HPy** crystallite after the rinsing.

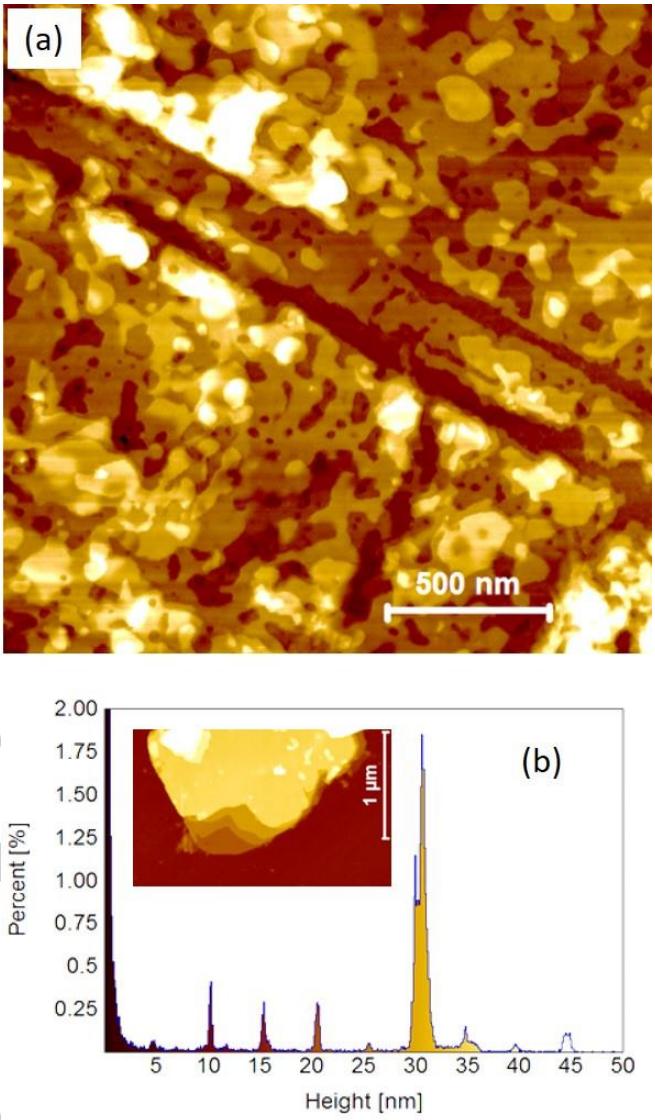

Figure 7. (a) AFM images captured on sample B after 18h soxhlet rinsing in ETOH. **(b)** Height histogram corresponding to the island shown in insert. Note the regular 5 nm step height.

Interestingly, in the case of sample B the AFM characterizations after rinsing revealed the existence of ultrathin 2D layers/extended islands at some surface locations (thickness ≤ 50 nm), exhibiting very characteristic structural features. The images show a structure made of flat and smooth terraces separated by regular 5 nm-high steps (**Fig.7**).

Discussion

The Fe-BDC system is a highly complex system since different structural phases, rigid or flexible, micro or mesoporous, can be obtained from the same precursors, namely Fe^{3+} and 1,4-BDC. In homogeneous phase, specific synthesis procedures have been developed to favor the selective formation of one target phase. Even though the structural characterizations generally confirm the majority formation of the desired phase, the competitive formation of other structural phases cannot be totally discarded. Generally, the formation of secondary phases is difficult to detect because of their low amount and their possible elimination during the post-synthesis treatments (rinsing, activation). In our synthesis conditions, the co-nucleation and growth of several crystalline phases are clearly evidenced. A first evidence is provided by the SEM images that show crystalline structures with very different characteristic shapes. The specific shape/habits of some crystallites gives direct insights on their structural properties/nature. This is the case for the hexagonal **HPy** and for the octahedral **O** crystallites whose 3D regular shapes are those expected for the hexagonal MOF-235 or MIL-88B phases and the cubic MIL-101 phase, respectively.

Other crystalline structures are also observed such as the 2D dense and faceted layer (**L**) observed in between the **HPy** on sample C (**Fig.1C-2**) and the **FP** crystallites exhibiting irregular hexagonal shape and variable orientations (**Fig.1A**). Their structural identification by XRD is made difficult due to the tiny amount of matter, orientation effects and the variability of the structural properties of some Fe-BDC structural phases (MIL-88B and MIL-53). In the following we first discuss the growth of the

hexagonal and cubic phases and then tentatively discuss the nature of the other crystalline structures.

Oriented growth of the hexagonal phase

Because of their regular hexagonal shape, the **HPy** crystallites can be identified as being one of the known hexagonal structures namely MIL-88B(Fe) or MOF-235. Their preferential orientation (c-axis perpendicular to the surface as observed on the SEM /AFM images) is consistent with the observation of only a couple of intense peaks at 2θ = 9.64° and 2θ = 19.35° on the XRD patterns (**Fig.4**) assigned to (002) and (004) Bragg reflections. The (001) texture is confirmed by the observation of other (00ℓ) Bragg peaks of superior order at greater angles (not shown). These peaks are always observed standing at the same angular position whatever the synthesis conditions indicating the formation of the same structural phase with the same crystalline parameters. Interestingly the structural characterization of material grown simultaneously in solution indicates the formation of the same phase in solution but with a different crystal shape (bi-pyramidal crystallites or hexagonal cylinders) (**Fig.SI-3**). The specific shape and orientation of the **HPy** therefore calls for their surface nucleation.

The closer structure in terms of peak position and relative intensity that can account for the obtained XRD patterns is that of MOF-235.[12] The observation of very reproducible peak positions for various samples prepared in different synthesis conditions is an additional argument in favor of the formation of this phase which corresponds to a rigid structure at the difference of the MIL-88B structure. Using the CIF file describing the MOF-235 structure and taking into account the reticular distances obtained in our experiments (from the XRD patterns corresponding to the **HPy** crystallites and the PXRD patterns of the same phase formed in solution) we could determine the structural parameters of the hexagonal phase obtained in our synthesis conditions. The structural parameters are: a = b = 12.74 Å, c = 18.32 Å, α = β = 90°, γ =120°, corresponding to a hexagonal structure with a unit cell volume of about 2575 Å^3 (space group: P -6 2 c). The calculated pattern corresponding to this structure is displayed **Fig.5** (blue pattern) and is compared to experimental XRD and PXRD patterns in **Fig.SI-3**. Further details about Bragg reflection indexes, peak positions and relative intensities can be found in Supporting Information (**Fig.SI-3, Fig.SI-4)**. The symmetry and the crystalline parameters were confirmed experimentally by complementary azimuthal out-of-plane XRD characterizations of the surface grown oriented **HPy** crystallites, giving access to Bragg reflections not measurable in Bragg Brentano configuration. The XRay source and detector positions were calculated taking into account the crystalline parameters of the structure and the (001) texture of the **HPy**. Examples of snapshot images of diffraction spots corresponding to (101), (202), (303), (211), (103) and (100) reflections are displayed in **Fig.SI-5**.

Comparatively to the other structural phases, the hexagonal crystallites **HPy** are stable in DMF (the solvent used for the synthesis) but are easily peeled off or damaged upon rinsing in hot EtOH. Their almost total disappearance after rinsing in a protic solvent like EtOH indicates a weak surface connection.

A stronger anchoring of some crystallites is however evidenced, as stated by the observation of few **HPy** crystallites as well as residual fragments of the former crystallites still present on the surface after rinsing (**Fig.6b**, **Fig.SI-4**). For the oriented **HPy** still present on the surface, the SEM images reveal a decrease of their lateral size (**Fig.6c insert**). Quantitatively a simple geometrical calculation gives a lateral size reduction of $\Delta a = \Delta b \sim -16\%$ in agreement with the crystalline network deformations reported for the MIL-88B structure (see **Fig.8**).

In close correlation with the disappearance of most of the **HPy** crystallites evidenced on the SEM images, the XRD patterns reveal also a decrease of the (00ℓ) peaks assigned to these crystallites or their total disappearance. The diminution of the peak intensity is correlated to the observation of a new pair of (00ℓ) peaks of weaker intensity appearing at lower angles. Examples of XRD patterns measured on different samples prior to and after EtOH rinsing are displayed in SI (**Fig.SI-4**). In all cases, our results show that the new peaks appearing after the rinsing can be assigned to a MIL-88B(Fe) structure with structural parameters close to those of MIL-88B(Fe) dry form.[16a] In addition to the shift of the peaks, an evolution of the relative intensity I_{002}/I_{004} is also evidenced confirming the formation of a MIL-88B(Fe) structure (**Fig.SI-4.5**). The very reproducible peak position observed for the as-prepared **HPy** crystallites and the structural parameters - slightly differing from one sample to the other or depending on the rinsing protocol - after rinsing further sustain a structural transformation from a MOF-235 rigid structure into a flexible MIL- 88B(Fe) structure.

A comparison of the structural parameters of the phase obtained in our synthesis conditions with those reported in the literature for various hexagonal MIL-88B phases corresponding to different pore opening/filling is compiled in **Fig.8**.

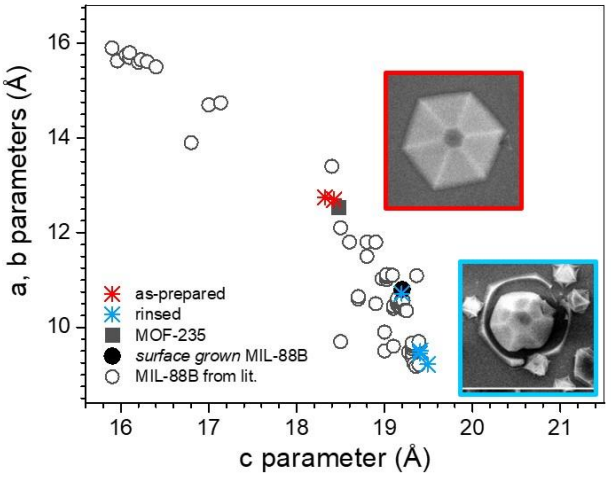

Figure 8. Evolution of (a, b) and c crystalline parameters of the flexible Fe-BDC hexagonal phase. The crystalline parameters of the as-prepared crystallites (red stars) or after EtOH rinsing (blue stars) are compared to those reported in the literature for various hexagonal structures. The black square (■) and dot (●) correspond to the closest hexagonal structures i.e. MOF-235 (■)[12] and *surface grown* MIL-88B (●)[16c, 22]. The open black circles (○) correspond to data collected in the literature, corresponding to different MIL-88B phase with variable pore opening or filling.[11, 16a, 16b] SEM images of **HPy** before and after ETOH rinsing are also shown: the lateral shrinkage of about 16% observed after rinsing is consistent with the evolution of (a=b) parameters inferred from XRD.

The parameters determined for the *as-prepared* samples (red stars) and *after rinsing* (cyan stars) match well those reported in the literature. The structural variations observed experimentally after rinsing (lateral shrinkage of the hexagonal pyramids and increase of the c lattice parameter) are consistent with the

variations of the lattice parameters reported upon solvent release/drying of MIL-88B phases.[16a] They correspond to a decrease of the volume of the unit cell from ~2575 Å^3 (*as-prepared*) to ~1430 Å^3 after rinsing.

Our studies show that the growth of the **HPy** crystallites is promoted by BDC excess in solution and solely observed on Si-COOH surfaces. These results are in agreements with studies reported in the literature showing the preferential growth of MIL-88B(Fe) above a certain BDC concentration threshold, in case of synthesis in homogeneous phase.[28] In conditions of excess BDC concentration, it may be figured out that the growth mechanism proceeds through the formation of BDC stabilized Fe µ3-oxo clusters in solution and their subsequent assembly to form the hexagonal network. Growth mechanisms involving the formation of secondary building units (SBUs) are reported in the literature, in particular for surface growth of Cu-carboxylate MOF (HKUST).[29] According to such a scenario, the selective growth of this phase on Si-COOH surfaces could account for specific affinity of the BDC stabilized SBUs for the Si-COOH surface (**Fig.9a**). Surface interaction through hydrogen bonding may be figured out and might explain the weak surface anchoring of the hexagonal crystallites upon rinsing in EtOH.

As far as the nucleation takes place and even in conditions it is not favored (low nucleation rate), our results indicate that the hexagonal phase is quantitatively the most abundant phase on the surface thus indicating a much faster growth kinetics. The SEM images indicate a 3D growth of crystallites leading to the formation of dense layers of close-packed **HPy** crystallites in condition of high nucleation rate. In these conditions the lateral growth is limited by the presence of neighbor crystallites. Neither crystallite merging nor surface recrystallization process was evidenced.

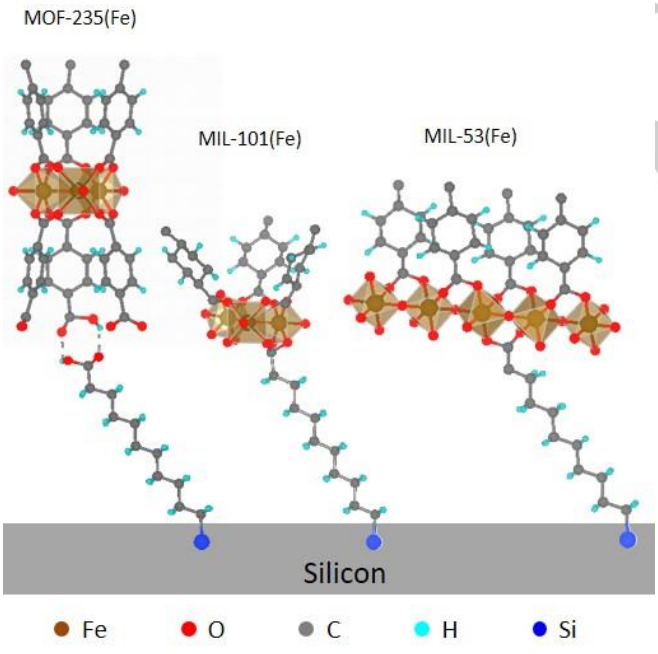

Figure 9. Proposed surface anchoring of the different crystalline phases: through hydrogen bonding of BDC stabilized Fe µ3-oxo clusters for the hexagonal MOF-235 **HPy** crystallites, through coordination linkage of the Fe µ3-oxo clusters or Fe-O-Fe chains for the MIL-101(Fe) and MIL-53(Fe) phases respectively

MIL-101 cubic phase

The growth of MIL-101(Fe) is supported by several results. The observation of crystallites with octahedral shape characteristic of cubic structures is a first indication of the formation of this structural phase which is the sole known Fe-BDC phase exhibiting this symmetry. The SEM images show that most often the MIL-101(Fe) octahedra are sitting on one of their (111) facets (**Fig.SI-6**). This specific orientation is in agreement with XRD patterns showing mainly (111) peak family corresponding to this phase. The 3D regular shape of the octahedra and the formation of the same type of octahedral crystallites with similar size distribution in solution call for their nucleation in homogeneous phase and their subsequent deposition on the surface. Their strong anchoring and the observation of crystallite merging together, leading to the formation of 2D islands indicate however the occurrence of surface reactions or re-crystallization processes of this metastable phase.

Other results call however for surface nucleation. First piece of evidence is the observation of **TPy** and **TP** particles (**Fig.1 B2**). Qualitatively, their regular shape - equilateral triangles or tetrahedral pyramids - is consistent with the crystal shape expected for a cubic structure. Their aspect ratio (mean thickness around 100 nm and lateral size of several hundreds of nm) however differs from that of the 3D regular octahedra. The shape/symmetry similarities of **TP** and **TPy** with **O** crystallites strongly call for a same and single phase but their differing aspect ratio suggests a surface nucleation process rather than their nucleation in homogeneous phase. Other pieces of evidence of surface growth/re-crystallization process is provided by AFM characterizations. The observation of nm-size 2D particles exhibiting a pore network on their topmost surface (**Fig.3**) as well as 2D ultrathin layer exhibiting flat terraces separated by regular steps (**Fig.7**) is in agreement with such a scenario. The hexagonal symmetry of the pore network and the mean pore distance ~ 6 nm observed on the 2D nano-crystallites is in good agreement with the 2D organization of pores in (111) planes of the MIL-101 structure. The zeotype architecture of MIL-101 is illustrated in **Fig.10.** The structure corresponds to a cubic network involving two types of cages (pores): “large” cages (grey color) and “small” cages (green color) (**Fig.10a**). Their envelopes are delimited by a grid network of Fe_3O oxo clusters (blue dots) interconnected by BDC linkers (grey sticks). The position of the oxo cluster nodes was determined on the basis of the atomic position given in the MIL-101 CIF file[10], using a home-made calculation tool. The 3D cubic arrangement of the large cages (4 x 4 unit cells) is displayed in **Fig.10b**. Only the large cages are represented for the sake of clarity. In (111) planes these cages are organized according to a 2D hexagonal network with a lattice parameter of 6.3 nm (blue cages). The image **Fig.10d-f** show the structure/composition of selected (111) planes (1.6 nm thick slices) located at different levels along the [111] axis. The levels corresponding to the different (111) slices are indicated on **Fig.10c**. The reference level z0 is set at the bottom of the large cages forming the first stage. z1 and z2 correspond to (111) planes located in the middle of large cages located in the first (z1 = +1.4 nm) and second (z2 = +3.8 nm) stages. The slice at z3 = + 4.6 nm corresponds to a level closing the large cages (open windows at the top of the cages). When moving upwards (downwards) along the [111] axis variable composition is found corresponding to more or less dense surfaces. Open pores are found at many levels but their size /aperture are below the AFM resolution. Within one d_{111} reticular

distance the calculations show that a hexagonal network of pores similar to that observed experimentally on the AFM images is only found around z1 and z2 (**Fig.10e, f**).

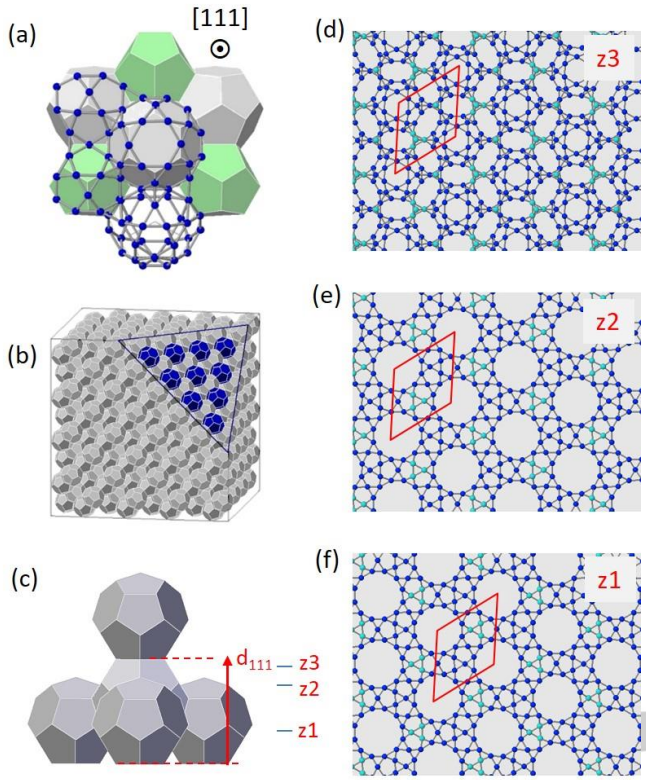

Figure 10. (a) Elementary zeolitic structure of the MIL 101 cubic phase constituted of "large" cages (grey color) and "small" cages (green color). The envelopes of the cages are delimited by Fe_3O oxo clusters (blue dots) interconnected by BDC linkers (grey sticks). **(b)** 3D scheme of the cubic network of the large cages (small cages are not represented for clarity). A corner of the cubic structure (4x4 unit cells) is truncated to show the hexagonal arrangement of the large cages in (111) plane (blue color). **(c)** Side view of the large cages stacking along the [111] axis. The reticular distance is d_{111} = 5.13 nm. **(d-f)** Calculated structure of (111) planes at different levels along [111] direction. The blue and green dots represent the Fe_3O oxo clusters involved in the envelops of large or small cages respectively. The reference plane is set arbitrarily at the bottom of the first stage of large cages. From top to bottom, the images show the structure of (111) planes at z3 = + 4.6 nm **(d)**, z2 = + 3.8nm **(e)** and z1 = + 1.4 nm **(f)** above the reference plane.

The observation of ultrathin 2D layers (thickness ≤ 50 nm) with flat terraces and regular steps (**Fig.7)** is an additional evidence of (111) oriented surface growth of the MIL-101 phase. Indeed, the regular step height of about 5 nm very close to the d_{111} reticular distance of the MIL-101 structure (d_{111} = 5.13 nm) allows for clearly identifying the nature of this structural phase despite the absence of any characteristic crystal shape. The thickness of the layers and their spatial extension (up to several tens of μm^2) strongly call for a surface dissolution/recristallization process leading to the formation of extended monocrystalline domains with (111) texture. The smoothness of the terraces could indicate a surface termination differing from that of the nano-crystallites above discussed. A lack of AFM tip resolution preventing the pore observation cannot be discarded however. Similar stair-case structure was reported recently in the case of MIL-100(Fe) single crystal deposited onto ITO thin layer on glass.[30] In this case also flat (111) terraces separated by ~4.5 nm high steps corresponding to the d_{111} reticular distance of the cubic MIL-100(Fe) structure were observed by AFM.

The stability of the MIL-101 phase upon rinsing suggests a surface anchoring through robust coordination linkages (**Fig. 9b**).

Nature of other crystalline phases

Besides the hexagonal and cubic phases, our results indicate also the growth of other crystalline structures: prism-like particles (**FP**) and dense faceted layers (**L**). Their nature is not trivial to identify simply on the basis of crystal shape considerations and/or from the XRD characterizations because of their small size/thickness and their coexistence with the other structural phases. A detailed analysis of SEM and XRD data show that the presence of these structures is correlated to the observation of a family of Bragg peaks standing at characteristic positions namely 2θ = 5.14°, 8.59°, 10.31°, 12.03°, 15.5°, 17.23° on the XRD patterns. These peaks are observed on the patterns of samples A and C (peaks with star labels in **Fig.5** and **Table 1**). Their positions match those expected for the (111) peak family of the MIL-101 phase (order 3, 5 and above) but their relative intensity with respect to the (222) peak (2θ = 3.43°) is several orders of magnitude greater than that expected (**Fig. SI-7**). This deviation allows for discarding they could correspond to this phase. Neither can their position account for a MIL-88B structure with different structural parameters. Indeed no matching is found neither with the XRD pattern of the as-prepared MOF-235 phase (rigid structure) nor with the MIL-88B phases obtained after rinsing (**Fig.SI-4**). The presence of these peaks suggests therefore the growth of a third structural phase.

The characteristic and irregular hexagonal shape of **FP** crystallites also strongly calls for the formation of a third structural phase. Their irregular facets and their angles *close to* but *differing* from 60° or 120° allow to discard they could correspond to hexagonal or cubic structures. Among the other known Fe-BDC phases, the formation of MIL-68 can be also discarded. Indeed, the positions of the peak family above mentioned do not match the XRD pattern of this orthorhombic phase.[14] In addition, the synthesis of this structural phase requires specific synthesis conditions differing from those used here (HCl addition, different Fe^{3+} precursors).[14] Hence the most likely hypothesis is the formation of a MIL-53 phase with a monoclinic or triclinic structure. Such symmetries may be reasonably assumed by analogy with the crystalline shape of monoclinic or triclinic natural minerals with crystal shapes very similar to that of the **FP** crystallites (**Fig.SI-8**). To confirm this hypothesis and get further insights on the structural parameters of this MIL-53 phase, the XRD patterns - restricted to the 6 peaks above mentioned - were fitted considering 3 different possible structures (monoclinic, triclinic and orthorhombic)[13b, 31]. The fitting was done by varying the different crystallographic parameters using a specifically developed home-made computing tool. The best fit was obtained for a monoclinic structure with the following crystallographic parameters a = 17.25 Å, b = 12.86 Å, c = 7.39 Å, α = 90°, β = 96°, γ = 90°. For this structure, the two most intense peaks at 2θ = 8.59° and 2θ = 10.31° correspond to (110) and (200) Bragg reflections, respectively. The other (less intense) peaks belong to the same peak families (superior order) except the peak at 2θ = 12.03° which corresponds to (001) Bragg reflection. The

experimental observation of two more intense peaks at $2\theta = 8.59°$ and $2\theta = 10.31°$ (**Fig.5** sample A) is perfectly consistent with the observation of two orientations of the **FP** crystallites: sitting on their largest facet or standing vertically (**Fig.1A**). Considering this peak family we could determine the type of structure (monoclinic) and the lattice parameters but not the symmetry group. The full resolution of the structural properties of this phase would require PXRD patterns of the pure phase to take into account the peak intensities.

The same family of peaks is also observed in the case of sample C indicating the formation of the same phase. In this case, no individual **FP** crystallite is observed on the SEM images. Two hypotheses can be raised. The peaks might be assigned to the continuous layer existing in between the hexagonal crystallites (**HPy**). The observation of **FP** crystallites merging together, leading to the formation of flat islands on A-type samples, would be consistent with the formation of more extended continuous layers in conditions of higher nucleation. Another possibility could be the presence of **FP** crystallites located underneath the **HPy** crystallites. Examples of **HPy** growing over pre-existing neighbor crystallites (octahedra or **FP** prisms) were observed on some samples.

The **FP** crystallites as well as the layer are resistant to rinsing suggesting a robust anchoring on the surface through coordination linkage (**Fig.9c**).

Conclusion

Fe-BDC MOFs were successfully grown onto silicon surfaces functionalized by an organic monolayer with –COOH tail groups, by direct exposure in DMF solutions containing variable Fe^{3+}/BDC precursor concentrations. The co-nucleation and growth of three different structural phases is evidenced and their nature and structural parameters were determined. The oriented growth of MIL-101(Fe) and one hexagonal phase with a structure close to MOF-235 is demonstrated as well as the growth of a third crystalline phase of MIL-53(Fe) type with a monoclinic structure. Compared to the other phases, the hexagonal phase exhibits remarkable features. Its oriented surface growth was only observed on Si-COOH functionalized surfaces suggesting that the presence of carboxylic acid ligands on the surface is a prerequisite for its nucleation. This phase exhibits however a much lower stability upon rinsing, revealing a weaker surface anchoring.

Particularly interesting and promising is the formation of extended 2D and textured ultrathin layers. Such layers of high crystalline quality and exhibiting extended monocrystalline domains open up interesting perspectives for the development of MOF-based integrated devices for which thin layers with low density of structural defects are required.

Experimental Section

Preparation of Si surfaces

The growth was carried out onto silicon surfaces with well controlled structure and surface chemistry. The samples were cut in monocrystalline Si(111) wafers (n-type, 0.2° miscut along [11$\bar{2}$] direction) then etched in oxygen free 40% NH_4F solution to remove the surface oxide layer and obtain hydrogenated terminated surfaces (H-Si). The etching procedure allows for obtaining H-Si(111) surfaces exhibiting extended (111) terraces flat at atomic scale well suited for high resolution AFM imaging.[32] The H-Si surfaces were then functionalized by covalent grafting of ω-functionalized alkyl monolayer with carboxylic acid tail-groups (Si-COOH surfaces).[23b, 23d] Other surface chemistries were also considered. Oxidized surfaces with OH terminal groups (Si-OH surfaces) were prepared by immersion of H-Si surfaces in H_2O_2/H_2SO_4 $[1:2]_{vol}$ piranha solution for 10 mn. Surfaces functionalized by pyridyl ligands (Si-Py surfaces) were prepared by covalent coupling of amino ethyl pyridine onto the Si-COOH surfaces.[33]

Growth of Fe/BDC MOFs

Fe^{3+} and BDC solutions were prepared separately by dissolving $FeCl_3$, $6H_2O$ (98%, Sigma-Aldrich) and 1,4-Benzene dicarboxylic acid (Terephtalic acid 99+%, Acros Organics) in DMF (RS grade, Carlo Erba). Each solution was homogenized by sonication 10 min at RT and afterwards mixed together just prior to the introduction of the Si sample. The Si samples were put vertically or face down in the reactor to minimize the deposition of particles grown in homogeneous phase. The growth was activated by conventional heating in an oil bath pre-heated at the desired temperature, under atmospheric pressure. The *as-prepared* MOF layers were rinsed successively 5 min in DMF then in ethanol (EtOH) at RT and blown dry. In some experiments additional rinsing was carried out using usual procedures reported in the literature to activate the Fe-BDC MOFs (removal of solvents or precursors trapped in the porous structure). The samples were immersed in the DMF or ETOH heated at 90° for 2h or rinsed using a Soxhlet set-up for several hours. After rinsing the samples were blown dry under Ar flow.

Characterizations

The structural properties of the Fe/BDC layers were characterized by SEM (Hitachi S-4800 FE-SEM), XRD (Bruker D8 Advance or Rigaku Smartlab diffractometers) and AFM (Agilent 5500 PicoSPM). Bragg Brentano XRD measurements were carried out on the Bruker D8 Advance diffractometer equipped with a high resolution LINXEYE XE-T detector. Measurements were performed using a variable divergence slit in order to probe a constant surface area over the angular range explored ($2° \leq 2\theta \leq 26°$), 1.5° Soller slits for primary and secondary beam and an automatic anti-scattering knife. Parallel beam in-plane and azimuthal out-of plane measurements were performed using a SMARTLAB diffractometer equipped with a Cu rotating anode and a HYPIX-3000 detector. Measurements were performed without monochromator in order to benefit of high photon flux. AFM characterizations were performed in AC-mode under N_2 atmosphere. Sharp silicon tips (nominal tip radius ≤ 10 nm) were used for high-resolution imaging. Images were captured in attractive force regime, where the tip is in very weak interaction with the surface so as to achieve high resolution and non-destructive imaging of soft materials.[34]

Acknowledgements

This work has been supported by a public grant overseen by the French National Research Agency (ANR) as part of the "Investissements d'Avenir" program (Labex Charmmmat, ANR-11-LABX-0039 -grant) and has benefited of funding from the "EDF Chaire for sustainable energy" at Institut Polytechnique de Paris (N. Soulmi's postdoc).

H. Yuan and W. Fu gratefully acknowledge the Chinese Scholarship Council for the funding of their PhD.

We thank P. Allongue, R. Cortes, F. Maroun, M. Poggi and S. Tusseau-Nenez for many fruitful discussions and technical support.

Keywords: MOF • Thin layer • functionalized silicon surface • surface growth • AFM

[1] (a) R. J. Kuppler, D. J. Timmons, Q.-R. Fang, J.-R. Li, T. A. Makal, M. D. Young, D. Yuan, D. Zhao, W. Zhuang, H.-C. Zhou, *Coordination Chemistry Reviews* **2009**, *253*, 3042-3066; (b) H.-C. Zhou, J. R. Long, O. M. Yaghi, *Chemical Reviews* **2012**, *112*, 673-674.

[2] (a) M. Rubio-Martinez, C. Avci-Camur, A. W. Thornton, I. Imaz, D. Maspoch, M. R. Hill, *Chem Soc Rev* **2017**, *46*, 3453-3480; (b) L. Zhong, J. Ding, J. Qian, M. Hong, *Coordination Chemistry Reviews* **2021**, *434*, 213804.

[3] (a) K. Adil, Y. Belmabkhout, R. S. Pillai, A. Cadiau, P. M. Bhatt, A. H. Assen, G. Maurin, M. Eddaoudi, *Chemical Society Reviews* **2017**, *46*, 3402-3430; (b) J.-R. Li, J. Sculley, H.-C. Zhou, *Chemical Reviews* **2012**, *112*, 869-932; (c) S. Qiu, M. Xue, G. Zhu, *Chemical Society Reviews* **2014**, *43*, 6116-6140; (d) M. P. Suh, H. J. Park, T. K. Prasad, D.-W. Lim, *Chemical Reviews* **2012**, *112*, 782-835; (e) K. Sumida, D. L. Rogow, J. A. Mason, T. M. McDonald, E. D. Bloch, Z. R. Herm, T.-H. Bae, J. R. Long, *Chemical Reviews* **2012**, *112*, 724-781; (f) B. VandeVoorde, B. Bueken, J. Denayer, D. DeVos*, Vol. 43*, **2014**, pp. 5766-5766-5788; (g) H. Wu, Q. Gong, D. H. Olson, J. Li, *Chemical Reviews* **2012**, *112*, 836-868; (h) D. H. Hong, H. S. Shim, J. Ha, H. R. Moon, *Bulletin of the Korean Chemical Society* **2021**, *42*, 956-969; (i) J. Li, P. M. Bhatt, J. Li, M. Eddaoudi, Y. Liu, *Advanced Materials* **2020**, *32*, 2002563.

[4] S. M. J. Rogge, A. Bavykina, J. Hajek, H. Garcia, A. I. Olivos-Suarez, A. Sepulveda-Escribano, A. Vimont, G. Clet, P. Bazin, F. Kapteijn, M. Daturi, E. V. Ramos-Fernandez, F. X. Llabres i Xamena, V. Van Speybroeck, J. Gascon, *Chemical Society Reviews* **2017**, *46*, 3134-3184.

[5] (a) N. S. Bobbitt, M. L. Mendonca, A. J. Howarth, T. Islamoglu, J. T. Hupp, O. K. Farha, R. Q. Snurr, *Chemical Society Reviews* **2017**, *46*, 3357-3385; (b) L. E. Kreno, K. Leong, O. K. Farha, M. Allendorf, R. P. Van Duyne, J. T. Hupp, *Chemical Reviews* **2012**, *112*, 1105-1125; (c) J. Lei, R. Qian, P. Ling, L. Cui, H. Ju, *TrAC Trends in Analytical Chemistry* **2014**, *58*, 71-78; (d) D. Liu, K. Lu, C. Poon, W. Lin, *Inorganic Chemistry* **2013**, *53*, 1916-1924; (e) W. P. Lustig, S. Mukherjee, N. D. Rudd, A. V. Desai, J. Li, S. K. Ghosh, *Chemical Society Reviews* **2017**, *46*, 3242-3285; (f) A. Bieniek, A. P. Terzyk, M. Wiśniewski, K. Roszek, P. Kowalczyk, L. Sarkisov, S. Keskin, K. Kaneko, *Progress in Materials Science* **2021**, *117*, 100743; (g) M. d. J. Velásquez-Hernández, M. Linares-Moreau, E. Astria, F. Carraro, M. Z. Alyami, N. M. Khashab, C. J. Sumby, C. J. Doonan, P. Falcaro, *Coordination Chemistry Reviews* **2021**, *429*, 213651; (h) N. Kajal, V. Singh, R. Gupta, S. Gautam, *Environmental Research* **2022**, *204*, 112320; (i) S. M. Majhi, A. Ali, P. Rai, Y. E. Greish, A. Alzamly, S. G. Surya, N. Qamhieh, S. T. Mahmoud, *Nanoscale Advances* **2022**, *4*, 697-732; (j) J.-X. Wang, J. Yin, O. Shekhah, O. M. Bakr, M. Eddaoudi, O. F. Mohammed, *ACS Appl. Mater. Interfaces* **2022**, *14*, 9970-9986.

[6] (a) M. Giménez-Marqués, T. Hidalgo, C. Serre, P. Horcajada, *Coordination Chemistry Reviews* **2016**, *307, Part 2*, 342-360; (b) P. Horcajada, R. Gref, T. Baati, P. K. Allan, G. Maurin, P. Couvreur, G. Férey, R. E. Morris, C. Serre, *Chemical Reviews* **2012**, *112*, 1232-1268; (c) S. Keskin, S. Kızılel, *Industrial & Engineering Chemistry Research* **2011**, *50*, 1799-1812; (d) X. Lian, Y. Fang, E. Joseph, Q. Wang, J. Li, S. Banerjee, C. Lollar, X. Wang, H.-C. Zhou, *Chemical Society Reviews* **2017**, *46*, 3386-3401; (e) H.-S. Wang, *Coordination Chemistry Reviews* **2017**, *349*, 139-155; (f) I. Abánades Lázaro, R. S. Forgan, *Coordination Chemistry Reviews* **2019**, *380*, 230-259.

[7] (a) M. D. Allendorf, A. Schwartzberg, V. Stavila, A. A. Talin, *Chem. Eur. J.* **2011**, *17*, 11372; bO. Shekhah, J. Liu, R. A. Fischer, C. Woll, *Chemical Society Reviews* **2011**, *40*, 1081-1106; (c) P. Falcaro, R. Ricco, C. M. Doherty, K. Liang, A. J. Hill, M. J. Styles, *Chemical Society Reviews* **2014**, *43*, 5513-5560; (d) I. Stassen, N. Burtch, A. Talin, P. Falcaro, M. Allendorf, R. Ameloot, *Chemical Society Reviews* **2017**, *46*, 3185-3241; (e) V. Stavila, A. A. Talin, M. D. Allendorf, *Chemical Society Reviews* **2014**, *43*, 5994-6010; (f) J.-L. Wang, C. Wang, W. Lin, *ACS Catalysis* **2012**, *2*, 2630-2640; (g) S. Chuhadiya, Himanshu, D. Suthar, S. L. Patel, M. S. Dhaka, *Coordination Chemistry Reviews* **2021**, *446*, 214115; (h) H. Kumar, R. Sharma, A. Yadav, R. Kumari, *Journal of Energy Storage* **2021**, *33*, 102032.

[8] A. Bétard, R. A. Fischer, *Chemical Reviews* **2012**, *112*, 1055-1083.

[9] E. Biemmi, C. Scherb, T. Bein, *Journal of the American Chemical Society* **2007**, *129*, 8054-8055.

[10] G. Férey, C. Mellot-Draznieks, C. Serre, F. Millange, J. Dutour, S. Surblé, I. Margiolaki, *Science* **2005**, *309*, 2040-2042.

[11] S. Surblé, C. Serre, C. Mellot-Draznieks, F. Millange, G. Férey, *Chemical Communications* **2006**, 284-286.

[12] A. C. Sudik, A. P. Côté, O. M. Yaghi, *Inorganic Chemistry* **2005**, *44*, 2998-3000.

[13] (a) F. Millange, C. Serre, G. Férey, *Chemical Communications* **2002**, 822-823; (b) F. Millange, N. Guillou, R. I. Walton, J.-M. Greneche, I. Margiolaki, G. Ferey, *Chemical Communications* **2008**, 4732-4734.

[14] A. Fateeva, P. Horcajada, T. Devic, C. Serre, J. Marrot, J.-M. Grenèche, M. Morcrette, J.-M. Tarascon, G. Maurin, G. Férey, *European Journal of Inorganic Chemistry* **2010**, *2010*, 3789-3794.

[15] D. Bara, E. G. Meekel, I. Pakamorė, C. Wilson, S. Ling, R. S. Forgan, *Mater. Horiz.* **2021**, 3377-3386.

[16] (a) C. Serre, C. Mellot-Draznieks, S. Surblé, N. Audebrand, Y. Filinchuk, G. Férey, *Science* **2007**, *315*, 1828; (b) P. Horcajada, F. Salles, S. Wuttke, T. Devic, D. Heurtaux, G. Maurin, A. Vimont, M. Daturi, O. David, E. Magnier, N. Stock, Y. Filinchuk, D. Popov, C. Riekel, G. Férey, C. Serre, *Journal of the American Chemical Society* **2011**, *133*, 17839-17847; (c) C. Scherb, R. Koehn, T. Bein, *J. Mater. Chem.* **2010**, *20*, 3046-3051.

[17] (a) M. Benzaqui, M. Wahiduzzaman, H. Zhao, M. R. Hasan, T. Steenhaut, A. Saad, J. Marrot, P. Normand, J.-M. Grenèche, N. Heymans, G. De Weireld, A. Tissot, W. Shepard, Y. Filinchuk, S. Hermans, F. Carn, M. Manlankowska, C. Téllez, J. Coronas, G. Maurin, N. Steunou, C. Serre, *Journal of Materials Chemistry*

A **2022**; (b) H. Liang, X. Jiao, C. Li, D. Chen, *Journal of Materials Chemistry A* **2018**, *6*, 334-341.

[18] (a) Y. Li, G. Hou, J. Yang, J. Xie, X. Yuan, H. Yang, M. Wang*, Vol. 6*, **2016**, pp. 16395-16395-16403; (b) F. Jing, R. Liang, J. Xiong, R. Chen, S. Zhang, Y. Li, L. Wu, *Applied Catalysis B: Environmental* **2017**, *206*, 9-15; (c) J.-J. Du, Y.-P. Yuan, J.-X. Sun, F.-M. Peng, X. Jiang, L.-G. Qiu, A.-J. Xie, Y.-H. Shen, J.-F. Zhu, *Journal of Hazardous Materials* **2011**, *190*, 945-951; (d) R. Liang, F. Jing, L. Shen, N. Qin, L. Wu, *Journal of Hazardous Materials* **2015**, *287*, 364-372; (e) C. Gecgel, U. B. Simsek, B. Gozmen, M. Turabik, *Journal of the Iranian Chemical Society* **2019**, *16*, 1735-1748; (f) S. Li, J. Cui, X. Wu, X. Zhang, Q. Hu, X. Hou, *Journal of Hazardous Materials* **2019**, *373*, 408-416.

[19] (a) L. Ai, L. Li, C. Zhang, J. Fu, J. Jiang, *Chemistry – A European Journal* **2013**, *19*, 15105-15108; (b) J. Jia, F. Xu, Z. Long, X. Hou, M. J. Sepaniak, *Chemical Communications* **2013**, *49*, 4670-4672; (c) N. Duyen Thi Cam, L. Hanh Thi Ngoc, D. Trung Sy, P. Van Thinh, T. Dai Lam, H. Van Thi Thanh, T. Thuan Van, N. Duy Chinh, N. Trinh Duy, B. Long Giang, H. Huynh Ky Phuong, D. Van Thuan, *Journal of Chemistry* **2019**, *2019*; (d) W. Xiong, G. Zeng, Z. Yang, Y. Zhou, C. Zhang, M. Cheng, Y. Liu, L. Hu, J. Wan, C. Zhou, R. Xu, X. Li, *Science of The Total Environment* **2018**, *627*, 235-244; (e) Y. Gao, S. Li, Y. Li, L. Yao, H. Zhang, **2017**, *202*, 165; (f) X. Donghua, M. Yue, G. Yue, Z. Hongjian, Z. Haimin, W. Guozhong, Z. Yunxia, Z. Huijun*, Vol. 5*, **2017**, pp. 23794-23794-23804.

[20] (a) J. Du, S. Xu, L. Sun, F. Li, *Chemical Communications* **2019**, *55*, 14773-14776; (b) H. Wang, X. He, W. Li, H. Chen, W. Fang, P. Tian, F. Xiao, L. Zhao, *Chemical Communications* **2019**, *55*, 11382-11385.

[21] (a) G. Ferey, F. Millange, M. Morcrette, C. Serre, M. L. Doublet, J. M. Greneche, J. M. Tarascon*, Vol. 46*, **2007**, pp. 3259-3259-3263; (b) C. Combelles, M. B. Yahia, L. Pedesseau, M. L. Doublet*, Vol. 114*, **2010**, pp. 9518-9518-9527.

[22] C. Scherb, A. Schödel, T. Bein, *Angewandte Chemie International Edition* **2008**, *47*, 5777-5779.

[23] (a) J. M. Buriak, *Chemical Reviews* **2002**, *102*, 1271-1308; (b) A. Faucheux, A. C. Gouget-Laemmel, C. H. de Villeneuve, R. Boukherroub, F. Ozanam, P. Allongue, J. N. Chazalviel, *Langmuir* **2006**, *22*, 153-162; (c) P. Gorostiza, C. H. de Villeneuve, Q. Y. Sun, F. Sanz, X. Wallart, R. Boukherroub, P. Allongue, *Journal of Physical Chemistry B* **2006**, *110*, 5576-5585; (d) C. Henry-de-Villeneuve, T. L. Nguyen-Le, F. Ozanam, P. Allongue, *Langmuir* **2019**, *35*, 2547-2553.

[24] (a) A. Faucheux, A. C. Gouget-Laemmel, P. Allongue, C. H. de Villeneuve, F. Ozanam, J. N. Chazalviel, *Langmuir* **2007**, *23*, 1326-1332; (b) A. Faucheux, F. Yang, P. Allongue, C. H. De Villeneuve, F. Ozanam, J. N. Chazalviel, *Applied Physics Letters* **2006**, *88*.

[25] L. Lu, PhD thesis, Ecole Polytechnique, https://pastel.archives-ouvertes.fr/pastel-01058915 **2014**.

[26] (a) H. Z. Yu, S. Morin, D. D. M. Wayner, P. Allongue, C. H. de Villeneuve, *Journal of Physical Chemistry B* **2000**, *104*, 11157-11161; (b) X. Wallart, C. H. de Villeneuve, P. Allongue, *Journal of the American Chemical Society* **2005**, *127*, 7871-7878.

[27] H. Yuan, PhD thesis, Université Paris Saclay (COmUE), https://pastel.archives-ouvertes.fr/tel-01680169, **2017**.

[28] M. Ma, A. Bétard, I. Weber, N. S. Al-Hokbany, R. A. Fischer, N. Metzler-Nolte, *Crystal Growth & Design* **2013**, *13*, 2286-2291.

[29] V. Stavila, J. Volponi, A. M. Katzenmeyer, M. C. Dixon, M. D. Allendorf, *Chemical Science* **2012**, *3*, 1531-1540.

[30] I. Christodoulou, T. Bourguignon, X. Li, G. Patriarche, C. Serre, C. Marlière, R. Gref, *Nanomaterials* **2021**, *11*, 722.

[31] T. R. Whitfield, X. Wang, L. Liu, A. J. Jacobson, *Solid State Sciences* **2005**, *7*, 1096-1103.

[32] P. Allongue, C. H. de Villeneuve, S. Morin, R. Boukherroub, D. D. M. Wayner, *Electrochimica Acta* **2000**, *45*, 4591-4598.

[33] L. Lu, Ph.D. thesis thesis, Ecole Polytechnique, Université Paris Saclay, Palaiseau, France **2014**.

[34] (a) R. Garcia, A. San Paulo, *Ultramicroscopy* **2000**, *82*, 79-83; (b) A. San Paulo, R. Garcia, *Biophysical Journal* **2000**, *78*, 1599-1605.

Entry for the Table of Contents

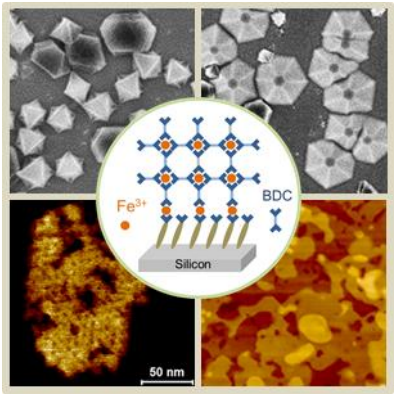

Fe/BDC MOFs are grown onto silicon surfaces functionalized with a carboxylic acid monolayer. The co-nucleation of different structural phases is evidenced whose nature and structural properties are determined based on SEM, XRD and high resolution AFM characterizations.